ORIGINAL ARTICLE

Anti-osteosarcoma trimodal synergistic therapy using NiFe-LDH and MXene nanocomposite for enhanced biocompatibility and efficacy

Yani Xu[a], **Lan Yang**[a], **Min Li**[a], **Haozhou Shu**[b], **Na Jia**[a], **Yunzhen Gao**[a], **Rongying Shi**[a], **Xiaojia Yang**[a], **Zhirong Zhang**[a], **Ling Zhang**[b,*]

[a]*Key Laboratory of Drug-Targeting and Drug Delivery System of the Education Ministry, West China School of Pharmacy, Sichuan University, Chengdu 610041, China*
[b]*Med-X Center for Materials, College of Polymer Science and Engineering, Sichuan University, Chengdu 610065, China*

Abstract   Osteosarcoma is usually resistant to immunotherapy and, thus primarily relies on surgical resection and high-dosage chemotherapy. Unfortunately, less invasive or toxic therapies such as photo-thermal therapy (PTT) and chemodynamic therapy (CDT) generally failed to show satisfactory out-comes. Adequate multimodal therapies with proper safety profiles may provide better solutions for osteosarcoma. Herein, a simple nanocomposite that synergistically combines CDT, PTT, and chemo-therapy for osteosarcoma treatment was fabricated. In this composite, small 2D NiFe-LDH flakes were processed into 3D hollow nanospheres *via* template methods to encapsulate 5-Fluorouracil (5-FU) with high loading capacity. The nanospheres were then adsorbed onto larger 2D Ti_3C_2 MXene monolayers and finally shielded by bovine serum albumin (BSA) to form 5-FU@NiFe-LDH/Ti_3C_2/BSA nanoplat-forms (5NiTiB). Both *in vitro* and *in vivo* data demonstrated that the 5-FU induced chemotherapy, NiFe-LDH driven chemodynamic effects, and MXene-based photothermal killing collectively exhib-ited a synergistic "all-in-one" anti-tumor effect. 5NiTiB improved tumor suppression rate from <5% by 5-FU alone to ∼80.1%. This nanotherapeutic platform achieved higher therapeutic efficacy with a lower agent dose, thereby minimizing side effects. Moreover, the composite is simple to produce, enabling the fine-tuning of dosages to suit different requirements. Thus, the platform is versatile and efficient, with potential for further development.

---

*Corresponding author.
   E-mail address: zhangling83@scu.edu.cn (Ling Zhang).

1. Introduction

Osteosarcoma, a primary malignant bone tumor, is distinguished by an elevated degree of genomic instability[1], which leads to disappointing outcomes with immune-checkpoint blockade (ICB) immunotherapy, conventional targeted therapy, and gene therapy[2−4]. Clinically, surgery combined with neoadjuvant chemotherapy remains the mainstream treatment option with a mere 60% survival rate[5], which is intricately linked to the systemic toxicity caused by high doses of chemotherapeutic drugs[6]. Currently, a variety of physical, chemical, and biological modalities have emerged for the management of osteosarcoma, including photothermal therapy (PTT), chemodynamic therapy (CDT), chemotherapy, etc. PTT, as an appealing non-invasive therapeutic modality, exerts its effects by selectively applying light to the tumor site, allowing for adjustable heat intensity and ultimately achieving tumor ablation[7,8]. For instance, Wang et al.[9] successfully synthesized 80 nm MoS_2 nanosheets and employed them in PTT against a 4T1 tumor model, leading to complete elimination of tumors. However, despite the efficient ablation of tumors, high-intensity and prolonged exposure during PTT may pose risks to the surrounding healthy tissues[10]. To circumvent this adverse effect, CDT is applied in the treatment of tumors, utilizing the products of the Fenton reaction to selectively kill tumor cells. By converting intracellular H_2O_2 into toxic hydroxyl radicals (·OH), CDT has the potential to overcome resistance mechanisms by inducing cytotoxic effects through different pathways[11,12], such as oxidative stress and disruption of cellular redox balance[13,14]. This unique ROS generation pattern enables CDT to circumvent the major obstacles of limited light penetration depth in PTT. Lin et al.[15] reported that copper peroxide (CP) nanodots could enhance CDT by self-supplying H_2O_2 and effectively inhibited tumor growth in U87MG-bearing mice. Although tumor cells harbor higher H_2O_2 levels compared to normal cells, the endogenous production of H_2O_2 is still insufficient to support CDT in generating the necessary amount of ROS, resulting in limited efficacy of CDT alone[16]. In addition, immunotherapy has demonstrated remarkable effectiveness in treating various types of tumors, including hepatocellular carcinoma, neuroblastoma, etc[17,18]. Research on immunotherapy for osteosarcoma has also emerged. However, due to the intrinsic heterogeneity of osteosarcoma, which contributes to its formidable nature, the current landscape of immunotherapy for osteosarcoma has yielded only modest advancements, whether utilizing cytotoxic T lymphocyte antigen-4 (CTLA-4) or anti-programmed death-1 (PD-1) antibodies[19].

The aforementioned monotherapies hold certain advantages, yet they also possess distinct limitations. Multimodal therapies have demonstrated favorable outcomes and become more widely studied[20,21]. However, the discourse surrounding the associated side effects of multimodal therapies remains insufficient. The establishment of an exemplary multimodal cancer therapy necessitates a delicate equilibrium between efficacy and safety management. To determine the fitting multimodal approach for tumor therapy, we have devised a methodology founded upon prior investigations via employing a combination of photothermal-chemodynamic-chemotherapy. Primarily, to mitigate the side effects of PTT, it is critical to employ materials with high photothermal conversion efficiency and superior biosafety. MXene exhibits efficient light absorption and heat conversion capability for PTT[22]. Moreover, the optical properties of 2D nanomaterials can be tuned by performing surface modifications. Zhu et al.[23] synthesized Ti-based MXene nanocomposites (Ti_3C_2Tx-Pt-PEG) by using Ti_3C_2 MXene nanosheets as a backbone with anchored platinum artificial nanozymes for tumor ablation. Another crucial aspect is the selection of a suitable material with the potential for chemodynamic therapy. NiFe-LDH, exhibiting strong catalyzing capability with Fe^{2+} through Fenton reactions. It is worth mentioning that NiFe-LDH possesses a unique layered structure and ion exchange capacity[24]. Its high surface area and porous structure could provide abundant adsorption sites for drug molecules[25]. To maximize its drug delivery potential, NiFe-LDH, a 2D material, can be transformed into 3D hollow nanospheres via the template method, thereby encapsulating chemotherapeutic drugs such as 5-Fluorouracil (5-FU) through ion exchange capacity and electrostatic adsorption. Additionally, NiFe-LDH exhibits alkaline properties and undergoes accelerated degradation in the slightly acidic tumor microenvironment[26], enabling pH-responsive drug release at the tumor site. This makes it an optimal carrier for chemotherapy drugs, and its inherent chemodynamic therapy can contribute to the anti-tumor effect as well. However, NiFe-LDH exhibits a positive charge in physiological environments, and numerous studies have demonstrated that the accumulation of positively charged nanoparticles may lead to significant side effects[27,28], which may be one of the reasons limiting the application of NiFe-LDH in the field of biomedicine. By simply electrostatically assembling 5-FU@NiFe-LDH nanoparticles with negatively charged Ti_3C_2 MXene, a nanocomposite that synergistically harnesses the potential of CDT, PTT, and chemotherapy is constructed, while its positive charge could be reduced simultaneously. Finally, a biocompatible outer layer of BSA is coated, effectively flipping the overall charge to negative and transforming it into a potentially safe and effective trimodal drug delivery platform for anti-osteosarcoma treatment.

For refractory cancer like osteosarcoma, it is imperative not only to combine multiple anti-tumor therapies but also to reasonably proportion them. In addition to pursuing effective osteosarcoma-killing effects, ensuring the safety of the combination therapy holds vital significance as well. In this study, we devised a multifunctional platform for synergistic tumor therapy, encompassing chemodynamic, photothermal, and chemotherapy modalities, to strike a harmonious balance between efficacy and safety. We explored the optimal drug ratios to achieve an equilibrium that maximizes therapeutic effects while minimizing undesirable side effects. As illustrated in Scheme 1, NiFe-LDH was processed from 2D flakes into 3D nanospheres with an internally loaded low dose of 5-FU, the hollowed nanospheres were subsequently attached to Ti_3C_2 MXene monolayers via simple electrostatic adsorption and finished with BSA coating to form 5-FU@NiFe-LDH/Ti_3C_2/BSA nanoplatforms (5NiTiB) in order to
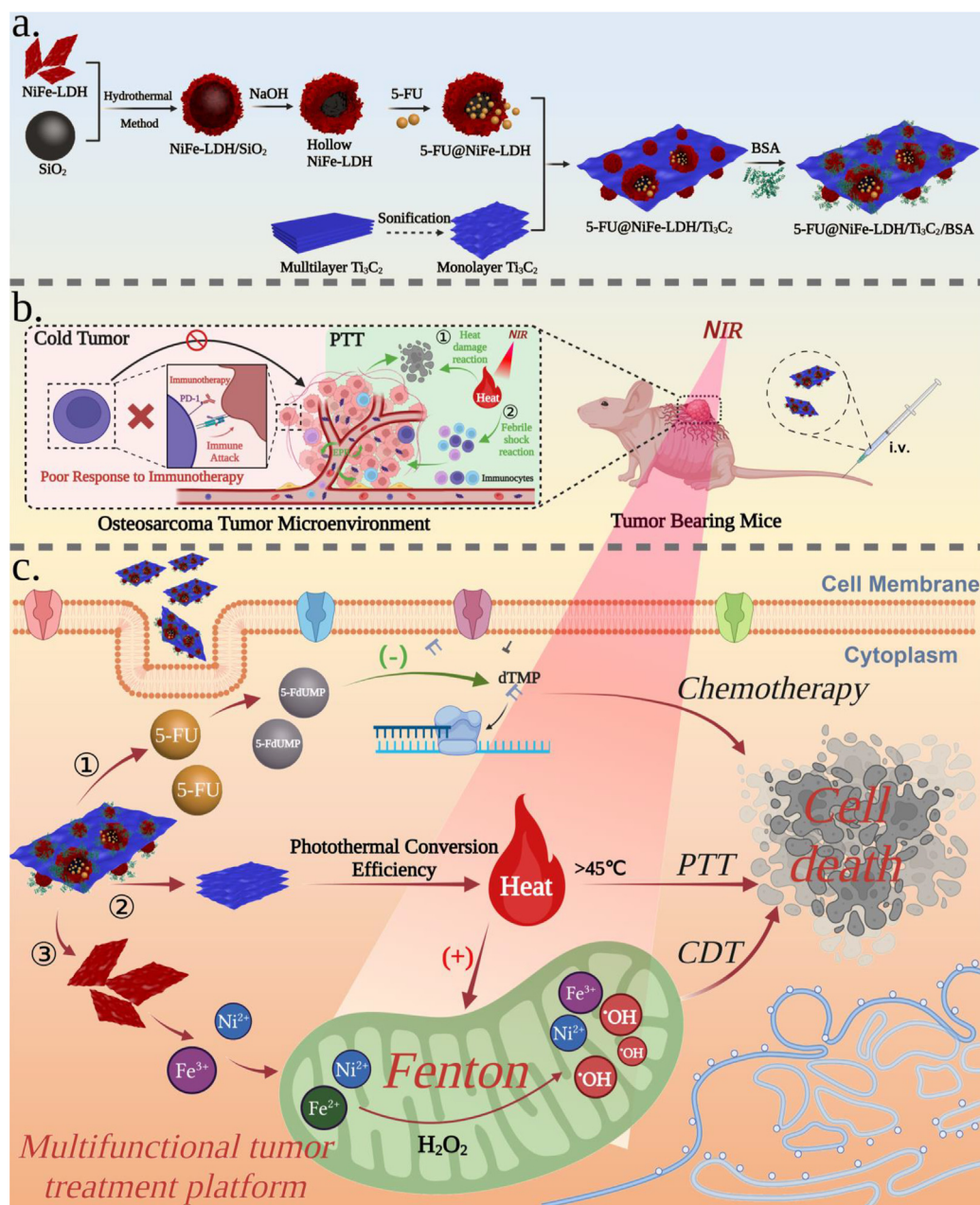
Scheme 1 Schematic illustration of the synergistic chemodynamic/photothermal/chemotherapy nano platform for osteosarcoma. 5-FU was loaded in hollow NiFe-LDH nanoparticles which were adsorbed onto 2D Ti_3C_2 MXene monolayers and then covered by BSA to form 5-FU@NiFe-LDH/Ti_3C_2/BSA nanoplatforms (5NiTiB), which exhibits "all-in-one" anti-tumor effects with NiFe-LDH-driven chemodynamic effects, MXene-based photothermal killing impacts, and 5-FU-induced chemotherapy.

improve compatibility and enhance uptake. This layer-by-layer wrapping *via* electrostatic adsorption gradually turned the positively charged NiFe-LDH nanospheres into negatively charged nanoplatforms, thereby increasing biocompatibility and reducing their systemic toxicity. Due to the designed pH-responsive drug release from hollow NiFe-LDH nanospheres, the acidic tumor microenvironment could trigger 5-FU accumulation in tumors, further reducing the systemic toxicity of 5-FU. Subsequent *in vitro* and *in vivo* experiments confirmed our hypothesis and defined that 5NiTiB possesses the most potent tumor inhibitory effect (over 16-fold increase of tumor suppression rate compared with 5-FU only) while maintaining a high level of biocompatibility and

systemic safety. To sum up, this study established a multifunctional trimodal therapeutic platform for osteosarcoma. First, the synergistic anti-tumor system enabled the mutually enhancing effect of PTT and CDT with pH-responsive controlled release of chemotherapy drug, through moderating the intensities, durations of PTT and doses of chemotherapy, a highly effective anti-tumor effect can be achieved while minimizing the toxic side effects of each therapeutic modality. Moreover, the ratio of different therapeutic modalities can be adjusted according to relevant tumor environments, so as to expand the possibilities of combined therapeutic solutions for more challenging-to-treat tumors, and ultimately achieve side-effect-free anti-tumor efficacy.

2.   Materials and methods

2.1.   Materials

Urea, hydrogen peroxide solution, ammonia solution, tetraethyl orthosilicate, ethanol, sodium hydroxide, nickel sulfate hexahydrate, and iron sulfate heptahydrate were procured from Aladdin Co., Ltd. (Shanghai, China). Tetramethylbenzidine, methyl blue aqueous solution, and glutathione were bought from Solarbio Co., Ltd. (Beijing, China).

2.2.   Animals and cell culture

Yaokang Biology (Chengdu, China) provided 18 ± 2 g, 6-week-old female BALB/c-nude mice. This study adhered to the regulations outlined in the National Laboratory Animal Use Law of China. The Institutional Animal Care and Ethics Committee of Sichuan University approved the housing conditions and procedures used, with approval number SYXK2023-0113. MNNG/HOS cells were maintained in 1640 complete medium with 10% FBS, and cultured at an unfluctuating temperature of 37 °C in a gas environment containing 5% CO_2.

2.3.   Synthesis of NiFe-LDH hollow nanospheres

Based on the optimized Stöber method[29], 40.5 mL of anhydrous ethanol and 12 mL of ammonia water were mixed, and 2.1 mL of TEOS was blended under agitating. After 1 h, the obtained liquid was under centrifugation in order to obtain sediment which was washed repeatedly. Finally, dry in an oven at 80 °C for 6 h to obtain solid SiO_2 powder. 30 mg of SiO_2 powder was dispersed in 35 mL of purified water. After ultrasonic treatment for 1 h, add nickel sulfate (0.6 mmol), ferrous sulfate (0.2 mmol), and urea (2.4 mmol) in turn, and stir the mixture in a magnetic mixer for 30 min. Then transfer the solution to react at 120 °C, after 12 h, collect the precipitate at the bottom. After repeated centrifugation and washing with deionized water, the NiFe-LDH/SiO_2 composite was acquired after drying. Finally, disperse an appropriate amount of the previous product in a sodium hydroxide solution (2 mol/L) and stir at ambient temperature for 12 h, the precipitate was obtained through centrifugation and subjected to two washes with deionized water. Subsequently, it was dried at a temperature of 80 °C for a duration of 6 h to acquire hollow NiFe-LDH nanospheres.

2.4.   Synthesis of 5-FU@NiFe-LDH NPs

NiFe-LDH hollow nanoparticles (10 mg) were dissolved in deionized water (5 mL) containing NaOH (400 mg) and 5-FU (4 mg). Stir at room temperature for 12 h, 5-FU@NiFe-LDH was obtained *via* centrifugation and washing.

2.5.   Synthesis and characterization of 5NiTiB

The prepared 5-FU@NiFe-LDH NPs were mixed and stirred with ultrasonic dispersed Ti_3C_2 material, and then dispersed in BSA alkaline solution (5 mL) and agitated for 40 min. The BSA-coated nanoparticles obtained through centrifugation were washed with purified water more than three times, and then naturally dehydrated and preserved at 4 °C for future utilization. The zeta potential, hydrated particle size, and polydispersity index (PDI) of nanoparticles were monitored using the Malvern

Zeta sizer (Nano ZS, Malvern Instruments Ltd., Malvern, WR, UK). Additionally, the size and morphology of 5NiTiB were assessed using Transmission Electron Microscopy (HITACHI HT7700 TEM, Hitachi Ltd., Tokyo, Japan). X-ray photoelectron spectroscopy (XPS) analysis was performed with AXIS Ultra DLD (Kratos Analytical, Manchester, UK). The nanoparticles were dispersed in PBS (pH 7.4) at 37 °C and specimens were taken at varied time points to measure the particle size, thereby assessing the physiological stability. The drug loading content (LC) and encapsulation efficiency (EE) of 5-FU were evaluated with an UV−Vis spectrophotometer (UV1900i, Shimadzu, Kyoto, Japan). LC and EE of 5NiTiB were calculated based on Eqs. (1) and (2):

$$LC_{5-FU} (\%) = (\text{Weight of 5-FU in NPs})/(\text{Weight of NPs}) \times 100 \tag{1}$$

$$EE_{5-FU} (\%) = (\text{Weight of 5-FU in NPs})/ \\ (\text{Weight of initial 5-FU}) \times 100 \tag{2}$$

2.6.   Dual-responsive drug release behavior triggered by pH and NIR

The release behaviors of 5-FU from 5NiTiB were assessed using the dialysis procedure. To gain a comprehensive understanding of the release behavior, four dialysis environments were provided, comprising of: (1) PBS (pH 6.0) with 808 nm laser irradiation, (2) PBS (pH 7.4) with 1 W/cm^2 laser irradiation, (3) PBS (pH 7.4) with 1.5 W/cm^2 laser irradiation, and (4) PBS (pH 7.4) with 2 W/cm^2 laser irradiation. Subsequently, the 5NiTiB (2 mg) was adjusted to 1 mg/mL by dilution, and 1 mL of this was dialyzed against 30 mL of dialysis media at the aforementioned conditions at 37 °C within a vortex bath. The amount of 5-FU released into the supernatant solutions was assessed at predefined time intervals *via* an UV−Vis spectrophotometer (Shimadzu).

2.7.   In vitro CDT effect

Experiments were carried out to monitor the generation of ROS through Fenton reactions to assess the chemical kinetic reactivity. Firstly, the degradation of methylene blue (MB) was employed for the detection of hydroxyl radical (·OH) generation. The synthesized material (50 μL, 100 μg/mL) was mixed with PBS solution containing 6 mmol/L of GSH, leading to the attainment of a final volume of 500 μL. After the incubation period of 1 h at a temperature of 37 °C, MB (100 μL, 100 μg/mL) and glucose (100 μL, 4 mg/mL) were added, followed by further incubation under 37 °C for various time points. The absorbance curves of MB were then measured by spectrophotometer (Shimadzu).

Next, the production of ·OH was assessed with 3,3′,5,5′-tetramethylbenzidine (TMB). H_2O_2 (50 mmol/L) was added to a TMB solution (0.8 mmol/L) containing the synthesized material (100 μg/mL). The absorbance was assessed at various time intervals using a spectrophotometer set at 650 nm to monitor the production of ·OH. To measure the production of singlet oxygen ($^1O_2$), 1,3-diphenylisobenzofuran (DPBF) served as a probe. DPBF reacts with $^1O_2$, leading to a decline in absorbance at 410 nm. The synthesized material (100 μg/mL) was mixed with DPIF dissolved in DMF (2 mg/mL), and subjected to laser for different durations, and the absorbance values were recorded. The

degradation of DPBF could be indirectly inferred from the changes in absorbance, as it represented the degradation of DPBF. In addition, the detection of $\cdot$OH was carried out through electron spin resonance (ESR). The synthesized material (100 µg/mL) was combined with a solution containing 5,5′-dimethyl-1-pyrroline N-oxide (DMPO) and PBS (pH 5.5), and added to a solution of H_2O_2 (50 mmol/L). The resulting mixture was placed in an ESR instrument to detect the signals and spectra of hydroxyl radicals.

2.8. Light conversion capacity of 5NiTiB

To assess the photothermal features, a suspension of 5NiTiB in water with a volume of 200 µL was prepared at 0, 50, 100, and 200 µg/mL, and was subjected to an 808 nm laser at 1.5 W/cm^2 for 480 s. To further examine the impact of power density on photothermal effectiveness, a dispersion of 5NiTiB at a concentration of 50 µg/mL was exposed to 0.5, 1, 1.5, and 2.0 W/cm^2 for 480 s. The temperature of the solution was continuously monitored by a thermal imaging camera (Testo 865, Testo, Schwarzwald, Germany) at specific intervals ranging from 0 to 8 min. Additionally, the variations in temperature of 5NiTiB were evaluated during repeated cycles of laser irradiation (808 nm, 1.5 W/cm^2) for a total of five on/off cycles. Furthermore, the photothermal conversion efficiency (η) of 5NiTiB was assessed using a previously reported method[30]. η was determined by applying Eq. (3):

$$\eta = \left(hS(T_{max} - T_{ssur}) - Q_{dis} \right) / I \left(1 - 10^{-A_{808}} \right) \tag{3}$$

where h represents the heat transfer coeffcient, S is the surface area of the container. T_{max} represents the steady-state temperature while T_{ssur} is the surrounding temperature. Q_{dis} is the energy absorbed, I is the power of incident laser power, and A_{808} is the absorbance at 808 nm.

2.9. Compatibility of 5NiTiB with RBC

RBCs at 10% hematocrit in 200 µL volume were used to conduct all the hemolysis assessments. In brief, RBCs were diluted in an erythrocyte buffer and subsequently combined with a range of concentrations of 5NiTiB. The resulting mixture was gently agitated using a vortex and then allowed to incubate at 37 °C for 4 h and centrifugate at a speed of 3500 rpm for 5 min. The light absorption of the supernatant at a wavelength of 541 nm was measured thereafter, using a 96-well plate by a multifunctional microplate reader (Tecan Infinite M200, Tecan, Durham, USA). The percentage of hemolysis was determined by employing Eq. (4):

Percent hemolysis (%) = (Sample absorbance−Negative control absorbance)/ (Positive control absorbance−Negative control absorbance) × 100 (4)

2.10. Cellular uptake

NiFe-LDH, NiFe-LDH/Ti$_3$C$_2$, and NiFe-LDH/Ti$_3$C$_2$/BSA containing the same amount of indocyanine green (ICG) were first synthesized for use in the following experiments. MNNG/HOS cells were seeded with a complete 1640 medium (10% FBS) and incubated overnight in a cell incubator. Subsequently, they were treated with blank 1640 medium and further incubated with NiFe-LDH, NiFe-LDH/Ti$_3$C$_2$, and NiFe-LDH/Ti$_3$C$_2$/BSA for 4 h, respectively. After the excess NiFe-LDH, NiFe-LDH/Ti$_3$C$_2$, and NiFe-LDH/Ti$_3$C$_2$/BSA were removed, the cells were subjected to three washes with PBS, and stained with DAPI for a duration of

10 min. Intracellular ICG fluorescence was used to investigate cellular uptake by a laser scanning confocal microscope LSM510 (Zeiss, Jena, Germany).

2.11. In vitro synergistic therapeutic efficacy

To evaluate the synergetic therapeutic efficacy of 5NiTiB, MNNG/HOS cells were maintained in a 5% CO$_2$ atmosphere at 37 °C overnight to ensure cellular adherence. Subsequently, free 5-FU, 5-FU@NiFe-LDH, 5-FU@NiFe-LDH/Ti$_3$C$_2$ (5NiTi), Ti$_3$C$_2$, 5NiTi, and 5NiTiB were added, with the last three groups irradiated with an 808 nm laser (2.0 W/cm2) for 2 min after the preparation's addition, cells without laser exposure and any additions were designated as the control group. Following 24 h incubation, all groups were treated with a Calcein/AM cell viability assay kit and CCK8 assay kit. Cell viability was observed and recorded using confocal microscopy LSM510 (Zeiss), and the live/death ratio was determined. In addition, to study the effect of formulation concentration, laser emission power density, and laser exposure time on the anti-tumor efficacy, the survival rates of MNNG/HOS cells in each group were analyzed using a single-factor analysis for different formulation concentrations, laser emission power, and laser exposure time after 24 h of treatment.

2.12. Cell apoptosis

Cell apoptosis in MNNG/HOS cells was assessed. Specifically, cells (1 × 105) were seeded overnight in a 6-well plate and subsequently subjected to different treatments: (1) Free 5-FU; (2) 5-FU@NiFe-LDH; (3) 5NiTi; (4) Ti$_3$C$_2$ + Laser; (5) 5NiTi + Laser and (6) 5NiTiB + Laser (In each group, "Laser" represents 808 nm Laser (2 W/cm^2, 2 min) except for separate emphasis groups). After 4 h, the cells were rinsed with PBS and subsequently treated with the mitochondrial membrane potential assay kit with JC-1 and analyzed using flow cytometry NovoCyte (Agilent Technologies, Santa Clara, CA, USA). In addition, the cells were plated on a confocal microscopy dish and imaged using a confocal microscope LSM510 (Zeiss) equipped with appropriate filters for JC-1 fluorescence.

2.13. In vitro tumor cell proliferation

Ki67 was utilized to evaluate the proliferative capacity of the cancer cells. MNNG/HOS cells were seeded and subjected to different treatments: (1) Free 5-FU; (2) 5-FU@NiFe-LDH; (3) 5NiTi; (4) Ti$_3$C$_2$ + Laser; (5) 5NiTi + Laser and (6) 5NiTiB + Laser. The cells were fixed on glass slides with xylene and rehydrated using incremental ethanol concentrations (100%, 95%, 70%, 50%). After blocking non-specific binding sites, the samples were incubated with the Ki67 primary antibody diluent overnight at 4 °C, afterwards, the cells were rinsed with PBS to eliminate any excess primary antibody. Subsequently, the samples were exposed to a CY3-conjugated secondary antibody and incubated for 1 h at ambient temperature, followed by PBS washing to eliminate any excess secondary antibody. Moreover, the nucleus and cytoskeleton were labeled using DAPI and actin-tracker Green-488.

2.14. In vivo antitumor effect and histology analysis

A subcutaneous tumor model of human osteosarcoma was established by subcutaneous injection of MNNG/HOS cells mixed with matrix gel in the axilla of BALB/c nude mice. (1 × 107 MNNG/HOS cells per mouse, 1:1 volume ratio of cell PBS resuspension

to highly concentrated matrix gel, subcutaneous injection volume of 100 μL per mouse) Upon the attainment of a tumor volume of 100mm3, the mice were allocated into six groups (five per group) randomly and subjected to different treatments: (1) PBS; (2) Free 5-FU; (3) 5-FU@NiFe-LDH; (4) 5NiTi; (5) 5NiTi + Laser and (6) 5NiTiB + Laser. The temperature of the tumor region was monitored. Additionally, the antitumor effects were evaluated. The tumor volumes were derived by applying Eq. (4) with the length of the longest axis (L) and the shortest axis (W) being measured:

$$V = 1/2 \left(LW^2 \right) \tag{5}$$

What's more, the tumor suppression rates of different treatment regimens were calculated to assess the anti-tumor efficacy. On Day 21, each group of mice was sacrificed, their osteosarcoma and major organs were dissected, and the tumors were measured in terms of weight and subjected to H&E staining to enable

microscopic visualization and histological examination. Moreover, the tumor sections were examined for cell death and tumor proliferation through TUNEL staining and Ki-67 immunohistochemistry.

2.15. Safety evaluation

BALB/c-nude mice were administrated with 5NiTiB (100 μL, 0.5 mmol/L) to determine the biocompatibility and the negative control group consisted of mice that were treated with PBS. After a corresponding 12-day treatment, subsequently euthanized, and their vital organs were harvested and subjected to H&E staining. The tissues were subsequently scrutinized under a light microscope (Axiovert 40CFL, Carl Zeiss, Jena, Germany) for histological analysis. Additionally, the body weights were documented to evaluate the extent of systemic toxicity induced by the formulation. On Day 12, blood was collected. The indexes of ALT,
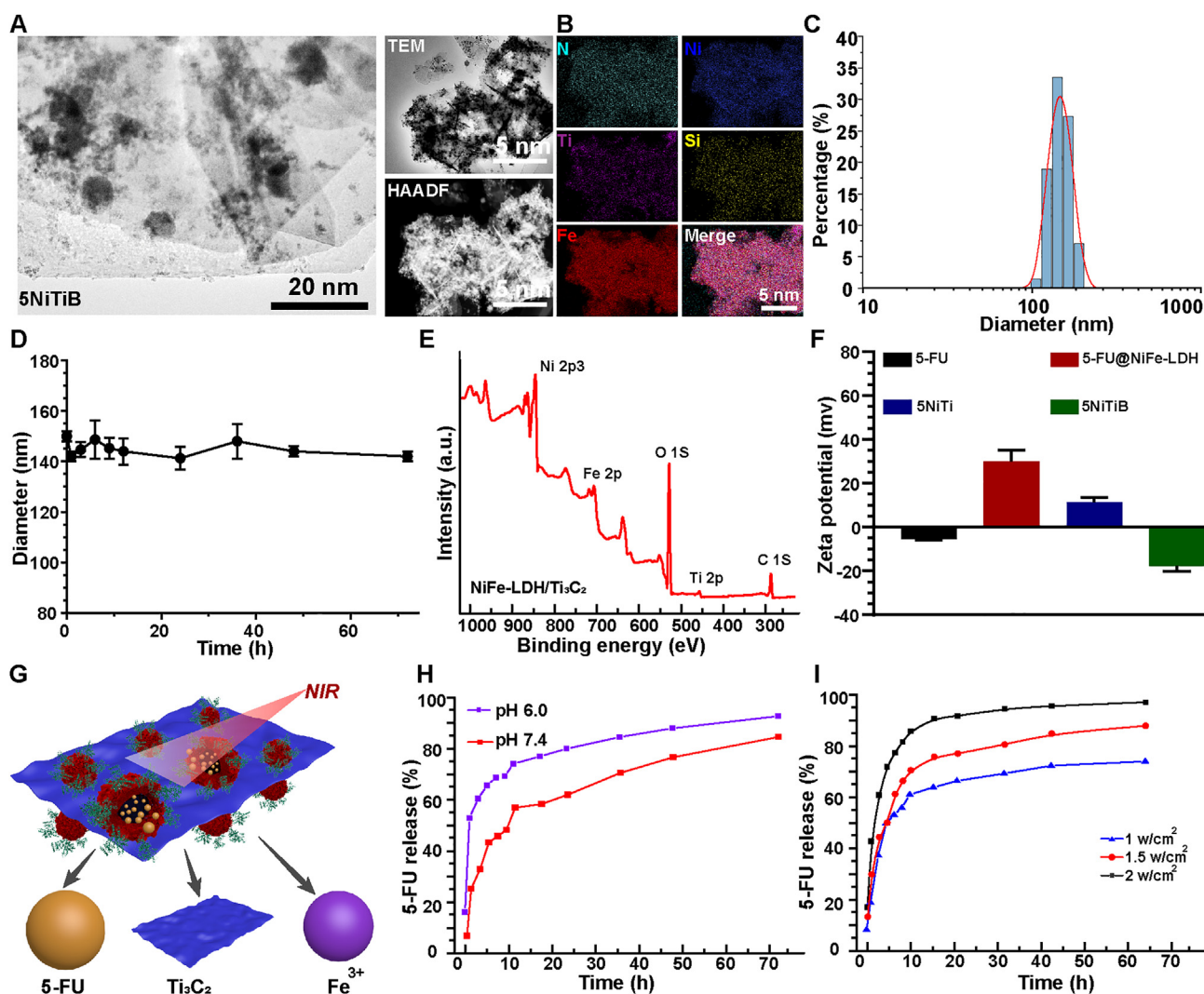

Figure 1 Preparation and characterization of 5-FU@NiFe-LDH/Ti$_3$C$_2$/BSA nanoplatforms (5NiTiB). (A) TEM images of 5NiTiB. Adsorbed 5-FU@NiFe-LDH are visible on the Ti$_3$C$_2$ layer. Scale bar, 20 nm. (B) TEM mapping of 5NiTiB. (C) Hydrodynamic diameter of 5NiTiB. (D) Physiological stability of 5NiTiB. Data are presented as mean ± SD ($n = 3$). (E) XPS spectra of NiFe-LDH/Ti$_3$C$_2$. (F) Zeta potentials of 5-FU, 5-FU@NiFe-LDH, 5-FU@NiFe-LDH/Ti$_3$C$_2$ (5NiTi) and 5NiTiB. (G) Upon near-infrared light irradiation, the various components of the nanoparticles exert chemotherapy effects, chemodynamic kinetics, and photothermal effects. (H) The release of 5-FU from the 5NiTiB under different pH conditions. (I) The release of 5-FU from the 5NiTiB under different laser emission densities.

AST, BUN, CR, ABL, and Globulin were detected by an automatic blood biochemical analyzer (Hitachi 7180 autoanalyzer, Japan Hitachi Ltd., Tokyo, Japan).

2.16. Statistical analysis

The statistical analysis of the data was carried out using the SPSS software (IBM SPSS Statistic 25). All data were presented as mean $\pm$ standard deviation (SD). One-way analysis of variance (ANOVA) was employed to assess the statistical significance of the results. An * for P-value <0.05 was considered statistically significant; ns, not significant.

3. Results and discussion

3.1. Preparation and characterization of 5NiTiB

First, NiFe-LDH/SiO_2 was synthesized on the surface of the SiO_2 microsphere using a co-precipitation method. NiFe-LDH hollow nanoparticles were obtained by removing internal SiO_2 nanoparticles with an alkaline buffer as NiFe-LDH is stable under this condition. The widely used chemotherapy drug, 5-FU, was then loaded into the hollow NiFe-LDH nanospheres due to the different charges carried by 5-FU and NiFe-LDH. Monolayered Ti_3C_2 MXene was prepared by sonicating multilayered MXene stock. Subsequently, the positively charged 5-FU@NiFe-LDH was again electrostatically adsorbed onto the negatively charged Ti_3C_2 monolayers, which were then coated with BSA (Scheme 1).

The morphology of 5NiTiB was examined. Clearly, spherical LDH nanoparticles with an average diameter of around 10 nm were adsorbed onto Ti_3C_2 MXene monolayers (Fig. 1A). The TEM mapping analysis showed the coexistence of Ni, Fe, Si and Ti elements, combined with the gradient potential change of nanoparticles (Fig. 1B and F). Consistently, XPS survey confirmed the simultaneous presence of the Ni, Fe, O, Ti, and C elements, indicating that LDH was indeed attached to the Ti_3C_2 nanosheets. The XPS results also indicated that Ni, Fe, and Ti were present in multiple forms in 5NiTiB (Fig. 1E, Supporting Information Fig. S1). These results demonstrated the successful synthesis of 5NiTiB. The hydrodynamic diameter of 5NiTiB was approximately 150 nm as measured by dynamic light scattering (Fig. 1C). Furthermore, the final nanocomposite appeared to be stable in PBS (pH 7.4), with only a small size change at 37 °C for 3 days (Fig. 1D). Subsequently, the standard method for measuring the concentration of 5-FU with UV spectrophotometer was established, LC and EE were calculated to be 10.79% and 90.5%, respectively (Supporting Information Fig. S2). Considering that after intravenous injection, the nanoparticles were transported from the blood to the slightly acidic tumor microenvironment[31], it is necessary to examine the release of the nanoparticles under these pH conditions. The results revealed that in PBS (pH 6.0), the release rate of 5-FU was faster compared to that in PBS (pH 7.4, Fig. 1H). This phenomenon may be attributed to the natural instability of NiFe-LDH under acidic conditions[32], which could trigger accelerated nanosphere disintegration and release of 5-FU. Therefore, the off-target toxicity of 5-FU may be reduced and the effective drug concentration at the tumor site may increase. Furthermore, to simulate the actual drug release environment
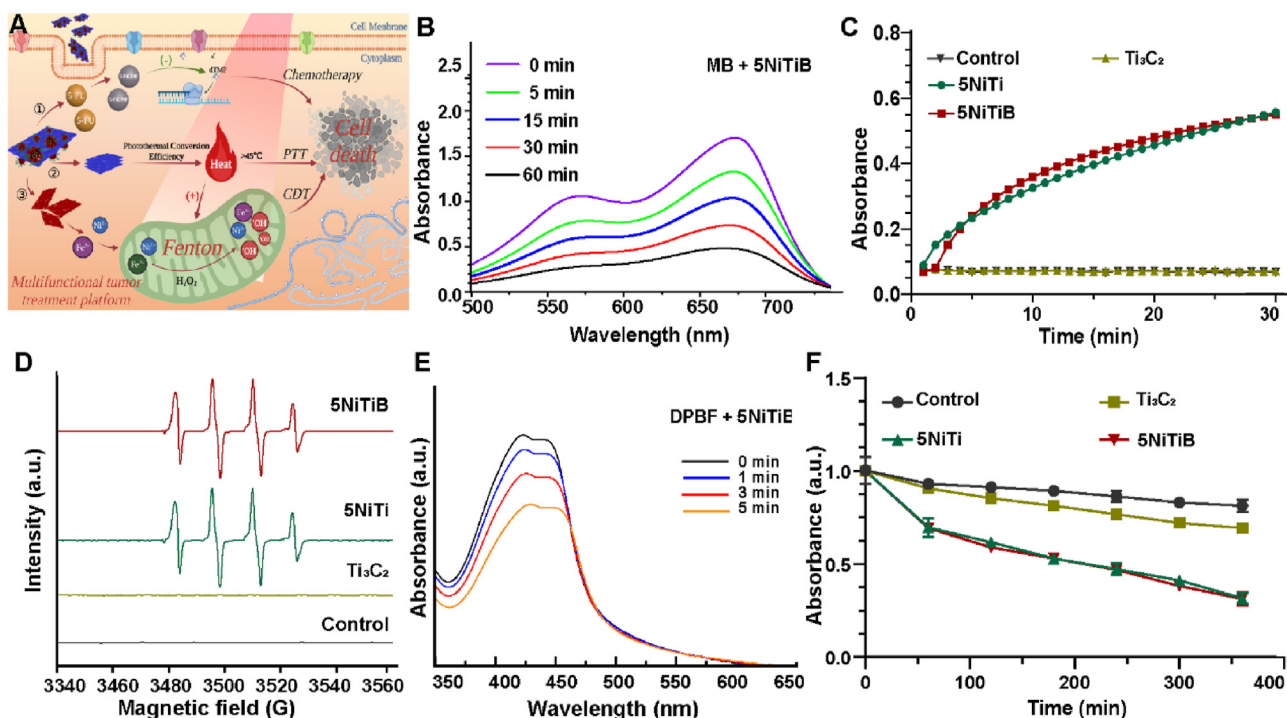

Figure 2 Chemodynamic properties of 5NiTiB. (A) Schematic illustration of the generation of ROS through Fenton reaction to exert CDT efficacy. (B) The degradation of methylene blue (MB) after incubating with 5NiTiB. (C) The generation of 3,3′,5, 5′-tetramethylbenzidine (TMB) after incubating with Ti_3C_2 MXene, 5NiTi, 5NiTiB. (D) The generation of hydroxyl radicals (•OH) after incubating with Ti_3C_2 MXene, 5NiTi and 5NiTiB. (E) The degradation of 1,3-diphenylisobenzofuran (DPBF) after incubating with 5NiTiB within 5 min. (F) The degradation of DPBF after incubating with Ti_3C_2 MXene, 5NiTi, and 5NiTiB. Data are presented as mean $\pm$ SD ($n = 3$).
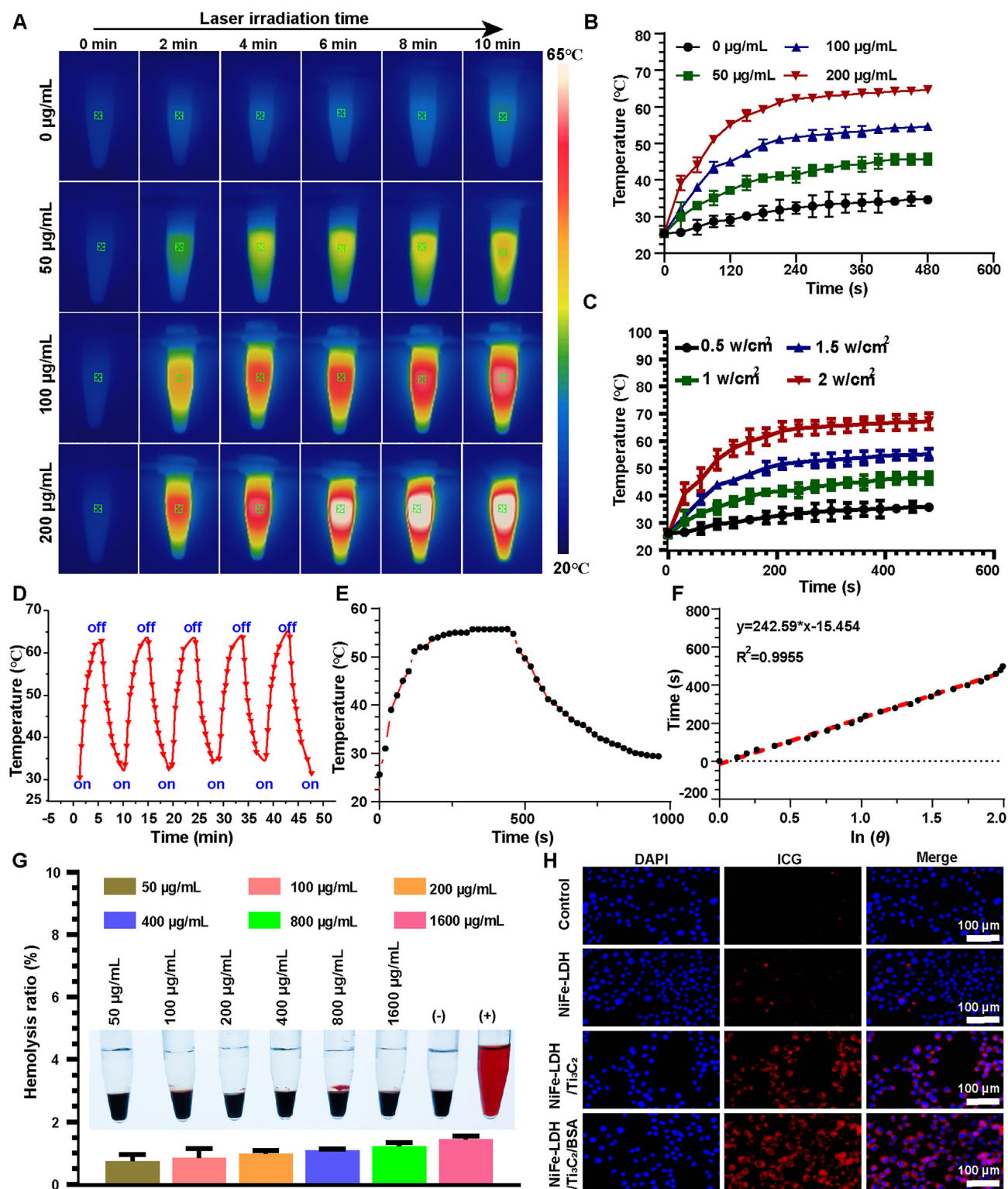
Figure 3 Photothermal capacity, blood compatibility, and cellular uptake of 5NiTiB. (A), (B) The thermal images in the infrared spectrum and the temporal changes of 5NiTiB at different concentrations were recorded during the application of NIR laser radiation (808 nm, 1.0 W/cm^2). Data are presented as mean ± SD (n = 3). (C) The photothermal effect of 5NiTiB (100 μg/mL) under varied power densities. Data are presented as mean ± SD (n = 3). (D) The photothermal durability of 5NiTiB during five rounds of NIR laser irradiation. (E) The process of gradually returning to room temperature after 8 min of laser irradiation cessation. (F) Standard curve of photothermal conversion efficiency. (G) Hemolysis evaluation of varying concentrations of 5NiTiB. Data are presented as mean ± SD (n = 3). (H) Fluorescence microscopy observations of MNNG/HOS cells after exposure to different formulations, scale bar = 100 μm.

during PTT, lasers with different power densities were employed to irradiate the prepared formulations. It was found that higher laser power resulted in a faster drug release rate (Fig. 1I). This may be attributed to the photothermal effect of Ti_3C_2 which increased the thermal motion of attached NiFe-LDH nanoparticles and facilitated the release of 5-FU.

In summary, the 5NiTiB nanocomposite is fabricated and briefly characterized. These nanostructures exhibited good stability and favorable drug release characteristics, which is adequate for further investigation. There have been a series of studies on the combined use of multiple 2D materials, but most of the preparation methods involved layer-by-layer stacking[33,34]. In our study,
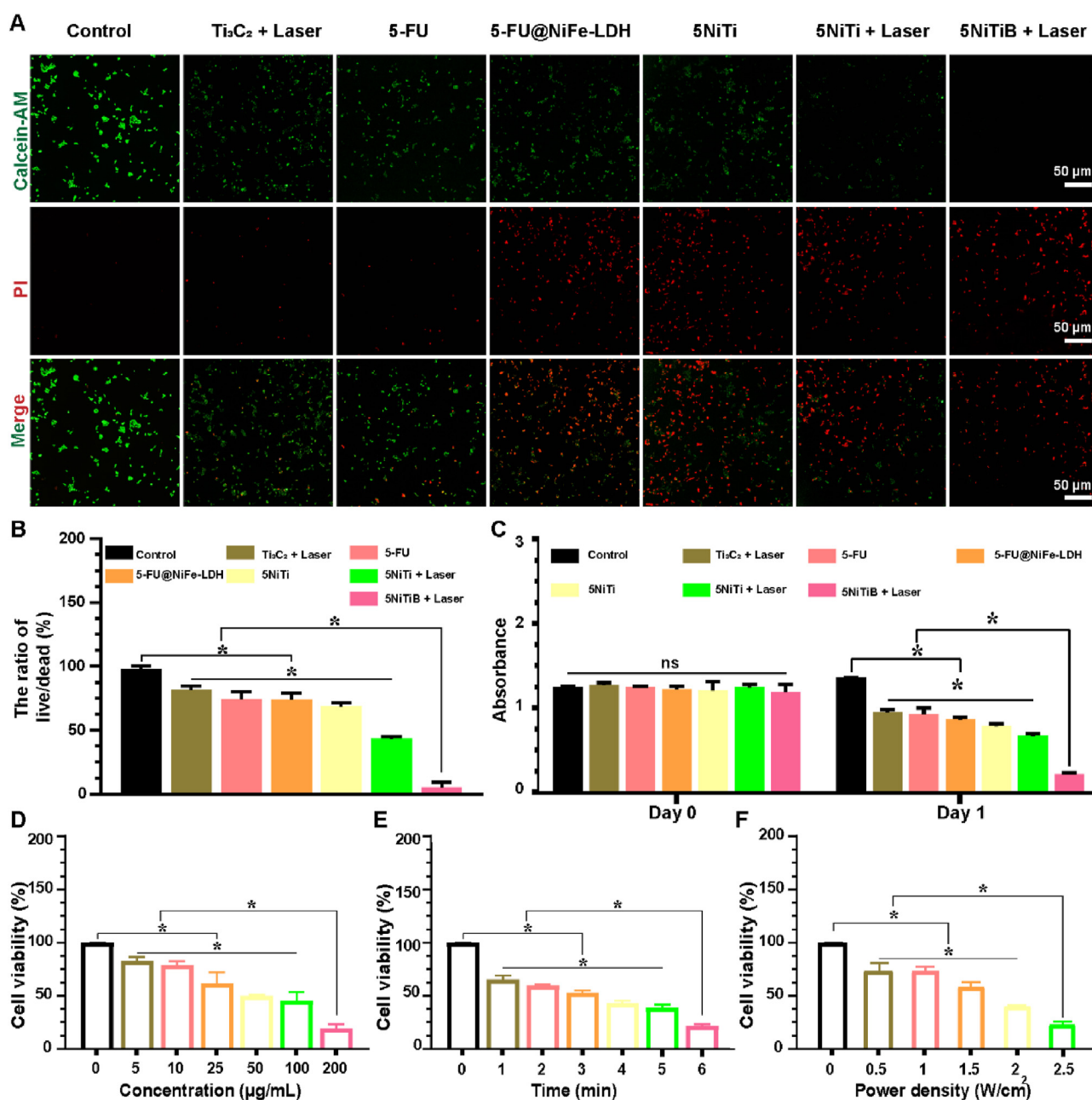

Figure 4 *In vitro* synergistic therapeutic efficacy of 5NiTiB. (A) Calcein-AM/PI staining images depicting MNNG/HOS cells following exposure to diverse formulations (Green fluorescence labels live cells, red fluorescence labels dead cells. Scale bar: 50 μm). (B) The ratio of live/dead MNNG/HOS cells after incubating with different formulations. Data are presented as mean ± SD ($n = 3$). *$P < 0.05$. (C) The absorbance of the CCK8 reagent solution after MNNG/HOS cells were incubated with different formulations. Data are presented as mean ± SD ($n = 3$). *$P < 0.05$. ns, not significant. (D) Cell viability of MNNG/HOS cells after incubating with 5NiTiB of different concentrations when exposed to laser (808 nm, 1 W/cm^2, 4 min). Data are presented as mean ± SD ($n = 3$). *$P < 0.05$. (E) The viability of MNNG/HOS cells was assessed by cell viability assays after incubating with 5NiTiB (100 μg/mL) when exposed to a laser (808 nm, 1 W/cm^2) for a different duration. Data are presented as mean ± SD ($n = 3$). *$P < 0.05$. (F) Cell viability of MNNG/HOS cells after incubating with 5NiTiB (100 μg/mL) when exposed to laser (808 nm) of different power densities. Data are presented as mean ± SD ($n = 3$). *$P < 0.05$.
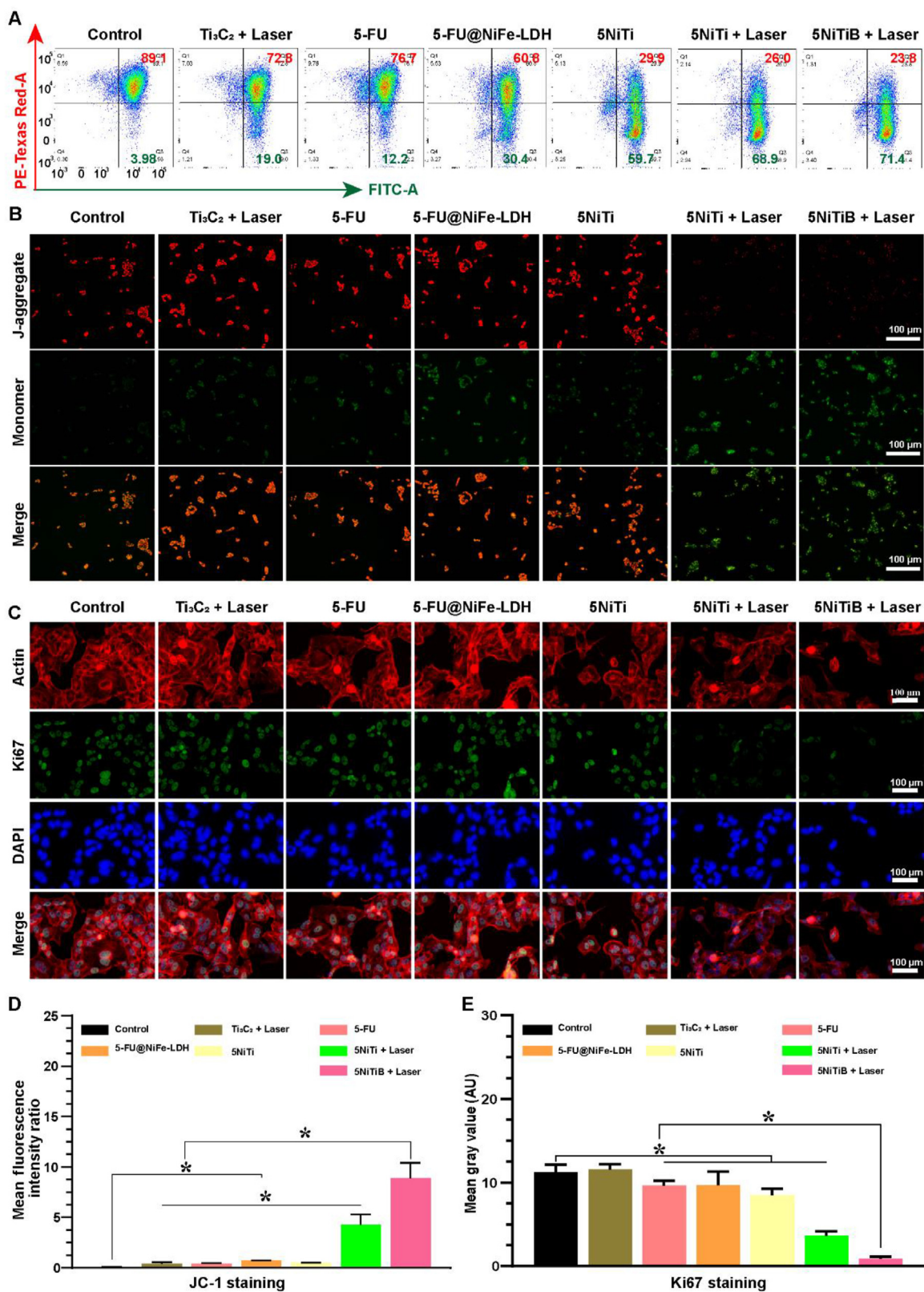
Figure 5 5NiTiB promotes apoptosis and inhibits recurrence of osteosarcoma. (A) Flow cytometry apoptosis experiment for JC-1 stained MNNG/HOS cells after implementing various approaches. (B) JC-1 staining images of MNNG/HOS cells after implementing approaches, scale bar = 100 μm. (C) Actin/Ki67/DAPI co-staining images of MNNG/HOS cells after applying different interventions, scale bar = 100 μm. (D) The mean fluorescence intensity ratio of MNNG/HOS cells after implementing various approaches. Data are presented as mean ± SD ($n = 3$). $*P < 0.05$. (E) Mean gray value of Actin/Ki67/DAPI co-stained MNNG/HOS cells after applying different interventions. Data are presented as mean ± SD ($n = 3$). $*P < 0.05$.
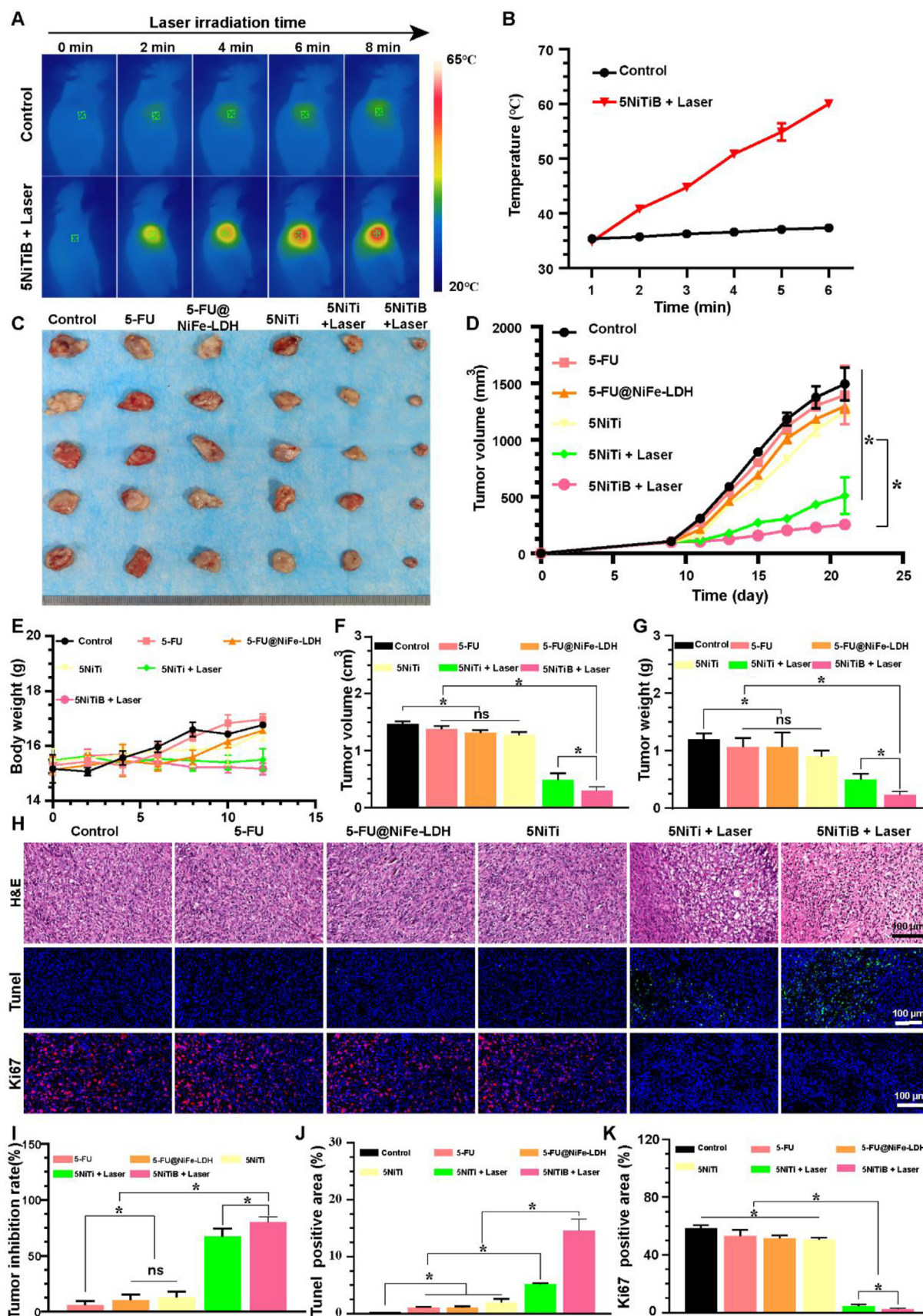
Figure 6 *In vivo* synergistic therapeutic efficacy of 5NiTiB. (A) *In vivo* photothermal effect of the 5NiTiB. (B) During an 808 nm laser irradiation for 6 min, the intravenous injection of PBS buffer and 5NiTiB into MNNG/HOS tumor-bearing mice was followed by captivating

we transformed the 2D LDH flakes into 3D nanospheres using SiO$_2$ as a template. By encapsulating drugs within the internal cavities, the nanospheres exhibited potential for tumor-specific responsive release. Furthermore, we adsorbed these nanospheres onto 2D Ti$_3$C$_2$ MXene flakes, which improved the stability of the LDH nanospheres and prevented aggregation due to their small size.

3.2. Chemodynamic efficacy of 5NiTiB in vitro

So far, LDH materials have been mostly used for the degradation of organic pollutants in water by catalyzing the Fenton reaction[35,36]. Their performance in cancer chemotherapy is yet to be investigated. As a start, MB, TMB, and DPBF were used as probes to measure the ROS/^{1}O$_2$ generation capability of our nanocomposites[37–39].

By monitoring the degree of MB degradation, it was found that the fabricated nanocomposites with or without final BSA modification (5NiTiB and 5NiTi, respectively) exhibited the highest level of MB degradation. Consistently, the light absorption of the TMB solution showed a significant increase in absorbance over time for the 5NiTi/5NiTiB, while remained relatively unchanged for the Ti$_3$C$_2$ control group (Fig. 2B and C). Unsurprisingly, by monitoring the changes in absorbance of DPBF, it was found that the 5NiTi/5NiTiB produced significantly more singlet oxygen (Fig. 2E and F). The ESR assessments also support that both 5NiTiB and 5NiTi nanocomposites exhibited the highest ROS generation (Fig. 2D). These results show that 5NiTiB and 5NiTi have the potential to be CDT agent, and further investigations are required.

3.3. Photothermal capacity of 5NiTiB in vitro

Photothermal conversion is another important aspect of the nanocomposite design. To test the photothermal capacity, the 5NiTiB solution was irradiated with an 808 nm laser. Meanwhile, the temperature was recorded every 30 s, and thermal images were captured. The temperature of the dispersed 5NiTiB showed clear concentration and time dependence (Fig. 3A–C). When the laser intensity, power density, and concentration were fixed, the temperature continued to increase with time. Normally, a photothermal temperature of 45 °C can meet the requirements of tumor killing and minimize the high-temperature damage to normal tissues[40]. It is important to carefully control the temperature and minimize the duration of laser irradiation while ensuring the effectiveness of thermal ablation for large-volume tumors. Therefore, the laser scheme for subsequent experiments was determined to be 2 W/cm^2, 50 μg/mL, and 2 min. In addition, the photothermal stability of 5NiTiB was determined using periodic NIR laser irradiation (2 W/cm^2, 2 min) for five consecutive cycles. It is worth noting that 5NiTiB showed outstanding photothermal stability after five cycles and η of 5NiTiB was calculated to be 36.7% (Fig. 3D–F).

3.4. Blood compatibility and cellular uptake of 5NiTiB

Blood compatibility is of great significance for the preparation which is administered directly into the bloodstream *via* the tail vein. Therefore, the hemolysis experiment was also conducted using deionized water as the positive control group. The results showed that hemolysis was not observed even at 1600 μg/mL, indicating that the preparation had excellent blood compatibility at the administered concentration and could be used for *in vivo* experiments (Fig. 3G). As the number of nanocomposites ingested by tumor cells increases, the tumor-killing effect potentially becomes greater. Therefore, the uptake of nanoparticles by MNNG/HOS cells was examined. ICG loaded in NiFe-LDH was used as a fluorescent marker to visualize the nanocomposites. It was found that the uptake of 5NiTiB coated with BSA was significantly increased by tumor cells (Fig. 3H). The reason might be that solid tumors require plenty of amino acids and energy during growth, of which albumin is one of the main sources[41]. Moreover, tumor cells express the albumin-binding receptor gp60 on their surface, which could assist the internalization of albumin-coated nanocomposites by enhancing caveolae-mediated endocytosis[42]. Then, the internalized cargoes may further bind to the albumin-binding protein SPARC and increase accumulation[43]. Therefore, the BSA coating on 5NiTi not only flipped the nanocomposite surface charge from positive to negative, reducing its toxicity but also increased its tumor cell uptake[44].

3.5. In vitro synergistic therapeutic efficacy of 5NiTiB

To validate the synergistic therapeutic effect of 5NiTiB on tumor cells, various formulations were applied on MNNG/HOS cells with laser irradiation, while MNNG/HOS cells treated with PBS served as the control group. Live cells and dead cells were distinguished, and the ratio was calculated (Fig. 4A and B). It was clearly visible that single chemotherapy with free 5-FU, single PTT with Ti$_3$C$_2$ + laser, and the combination of chemotherapy with CDT using 5-FU@NiFe-LDH only showed mild efficacy; whereas the efficacy of combination of CDT/PTT/CT with 5NiTiB + Laser was remarkably stronger. The results of the CCK8 cell viability assay also demonstrated a similar trend (Fig. 4C). Furthermore, the effects of formulation concentration, laser irradiation time, and laser intensity were evaluated through CCK8 experiments, as depicted in Fig. 4 D–F.

---

in vivo thermal imaging. Data are presented as mean ± SD ($n = 3$). (C) Images of tumors collected from mice on Day 21. (D) The fluctuations in tumor volume of MNNG/HOS tumor-bearing mice across various treatment groups during the period. Data are presented as mean ± SD ($n = 3$). *$P < 0.05$. (E) The fluctuations in body weight of MNNG/HOS tumor-bearing mice across various treatment groups during the treatment period. Data are presented as mean ± SD ($n = 3$). (F) Tumor volumes were measured after implementing various approaches on Day 21. Data are presented as mean ± SD ($n = 3$). *$P < 0.05$. ns, not significant. (G) Tumor weights were measured after implementing various approaches on Day 21. Data are presented as mean ± SD ($n = 3$). *$P < 0.05$. ns, not significant. (H) H&E, TUNEL, and antigen Ki67 immunohistochemistry of tumor slices in different groups, scale bar = 100 μm. (I) The tumor suppression rates of different treatment regimens. Data are presented as mean ± SD ($n = 3$). *$P < 0.05$. ns, not significant. (J) Tunel-positive area of tumor slices in different groups. Data are presented as mean ± SD ($n = 3$). *$P < 0.05$. (K) Ki67 positive area of tumor slices in different groups. Data are presented as mean ± SD ($n = 3$). *$P < 0.05$.

3.6. 5NiTiB promotes apoptosis and inhibits recurrence of osteosarcoma

Further apoptosis testing was also conducted, the mitochondrial membrane potential (MMP) in viable cells is elevated, and JC-1 accumulates within the mitochondrial matrix, forming cohesive aggregates that emit a crimson fluorescence. However, in apoptotic cells, MMP is reduced, and JC-1 exists as monomers emitting green fluorescence[45]. Observation of JC-1 treated MNNG/HOS cells using confocal microscopy qualitatively depicted the results of cell apoptosis (Fig. 5B), and the JC-1 flow cytometry results quantitatively demonstrated that treatment with free 5-FU alone induced apoptosis in merely 12.2% of tumor cells. In contrast, the application of 5NiTi resulted in a tumor cell survival rate of as low as 29.9%; while the treatment with 5NiTiB +808 nm laser resulted in only 23.8% of tumor cells surviving, with a high level of apoptosis rate up to 71.4%, making it the most effective group among all (Fig. 5A, C−E). We further assessed the effect of CDT by the detection of ROS levels (Supporting Information Fig. S4), and the addition of NiFe-LDH significantly increased ROS production, suggesting that CDT with NiFe-LDH produced an effect and that the large amount of ROS production in the tumor cells may be one of the causes of cell death after 5NiTiB treatment.

Due to the potentially severe adverse reactions caused by excessive chemotherapy drugs, the dosage of 5-FU encapsulated in this drug delivery system was reduced to ensure safety. The
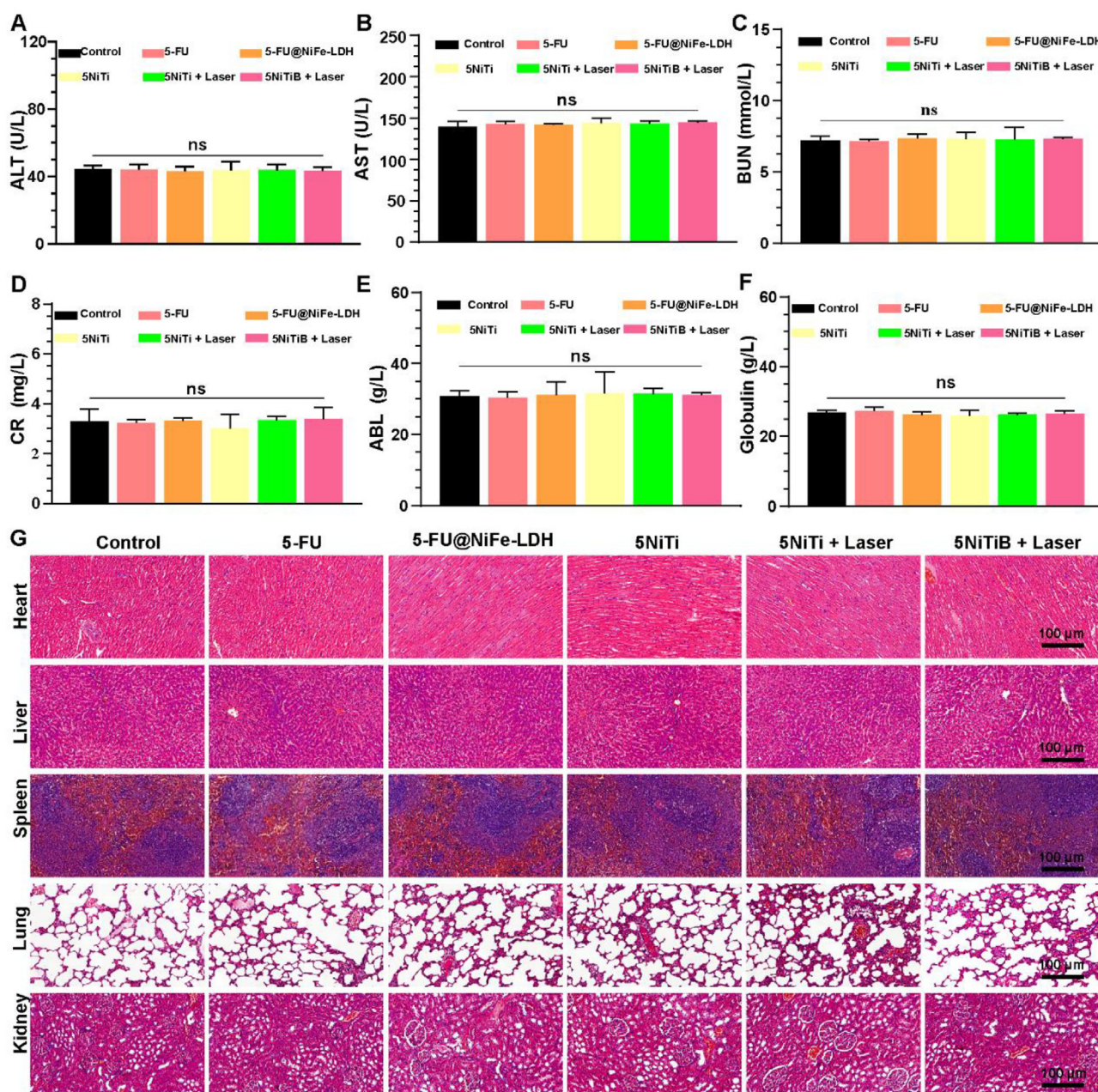

Figure 7 Safety evaluation of 5NiTiB. (A−F) The indexes of ALT, AST, BUN, CR, ABL, and Globulin of blood from BALB/c-nude mice treated with different formulations. Data are presented as mean ± SD ($n = 3$). ns, not significant. (G) H&E immunohistochemistry of major organ slices in every group, scale bar = 100 μm.

experimental results mentioned above collectively demonstrate that the use of 5-FU alone at lower doses is insufficient to maintain anti-tumor efficacy. However, the combined use of NiFe-LDH and Ti_3C_2 MXene significantly enhances the anti-tumor efficacy, thus achieving the goals in terms of therapeutic effectiveness.

3.7. In vivo synergistic therapeutic efficacy of 5NiTiB

To further investigate the efficacy of the designed anti-tumor drug delivery nano platform, an MNNG/HOS cell-bearing BALB/c-nude mouse model was established. The *in vivo* biodistribution of 5NiTiB labeled by CY5 and free CY5 was observed in tumor-bearing mice (Supporting Information Fig. S3). Free CY5 failed to accumulate in tumor sites, while 5NiTiB labeled by CY5 displayed tumor accumulation, whose reason might be that solid tumors require plenty of amino acids and energy during growth, of which albumin is one of the main sources[41]. Moreover, tumor cells express the albumin-binding receptor gp60 on their surface, which could assist the internalization of albumin-coated nanocomposites by enhancing caveolae-mediated endocytosis[42]. Then, the internalized cargoes may further bind to the albumin-binding protein SPARC and increase accumulation[43]. Following intravenous administration of different formulations, 808 nm laser irradiations were applied after 2 min; mice administrated with PBS served as control. Corresponding with the *in vitro* results, irradiation with 2 W/cm^2 yielded a progressive temperature increase at the tumorous site over time, and reached 45 °C after 2 min of irradiation, resulting in photothermal ablation of the tumor (Fig. 6A and B). The tumor volumes of the mice were monitored throughout the entire dosing period in Fig. 6D. The tumor volume and body weight of the mice were monitored throughout the entire period after implantation (Fig. 6D and E). Subsequently, after drug administration 4 times over 12 days, the volume and weight of excised tumors were measured (Fig. 6C and F and G). Reduction in tumor size was evident in groups treated with free 5-FU, 5-FU@NiFe-LDH, and 5NiTi, although no significant differences were detected between groups. The 808 nm laser irradiation strongly reduced the residual tumor volume and weight in the group of mice treated with 5NiTi and 5NiTiB, with the latter showing higher reduction. The tumor suppression rates illustrate that 5NiTiB offered the highest tumor suppression rate, with a remarkable increase from <5% by 5-FU only to 80.10% (Fig. 6I). The *in vivo* experimentation reaffirms the amalgamation of PTT and CDT as a veritable paradigm, ensuring not only the reduction in chemotherapeutic drug dosage but also the preservation of anti-tumor efficacy. Additionally, after 12 days of treatment, H&E, TUNEL, and Ki67 staining of tumor slices demonstrated that tumors with 5NiTiB +808 nm laser treatment exhibited severe tumor tissue necrosis, the most extensive degree of tumor apoptosis (marked by TUNEL), and the lowest level of proliferation (marked by Ki67) (Fig. 6I−K).

Besides, the *in vivo* biodistribution of 5NiTiB labeled by CY5 and free CY5 was observed in MNNG/HOS tumor-bearing mice (Supporting Information Fig. S5A). Free CY5 failed to accumulate in tumor sites, while 5NiTiB displayed tumor accumulation. The mice in each group were sacrificed at 6 h, the viscera were dissected out, and fluorescence imaging was performed, which showed that the 5NiTiB group did exhibit better tumor targeting ability (Fig. S5B).

In conclusion, treatment with 5NiTiB +808 nm laser effectively suppressed the growth of osteosarcoma, promoted tumor cell apoptosis, and inhibited tumor proliferation, thus inhibiting tumor recurrence. For hard-to-treat tumors like osteosarcoma only treated with high-dose chemotherapy in clinical practice, our primary focus is to reduce the dosage of chemotherapy drugs to minimize toxic side effects and ensure crucial safety. However, as indicated by the previous results, reducing the dosage of 5-FU inevitably leads to insufficient therapeutic efficacy. Fortunately, the trimodal drug delivery platform allows for the effective use of low-dose 5-FU while still ensuring excellent anti-tumor effects. The remaining aspect that needs to be validated is whether the approach of reducing chemotherapy drug dosage and restrained combined use of PTT and CDT can effectively reduce the adverse effects.

3.8. Safety evaluation

Upon administering the anti-tumor nanocomposites, major organs from mice were subjected to H&E staining, which yielded results that revealed no significant differences compared to the blank control group (Fig. 7G). Moreover, biochemical tests conducted on blood samples demonstrated no significant differences compared to the control group, therefore, the nanocomposites appeared to be biocompatible and passed the initial safety tests (Fig. 7A−F). As designed, multiple therapies were rationally proportioned by reducing the dosage of 5-FU, incorporating NiFe-LDH-loaded nanoparticles, synergistically employing Ti_3C_2 MXene, and controlling the intensity and duration of PTT. It is evident that the chemodynamic-photothermal-chemotherapy trimodal synergistic tumor therapy demonstrates a high level of safety.

4. Conclusions

In summary, a multicomponent nanocomposite with synergistic chemotherapy, chemodynamic, and photothermal effects for osteosarcoma treatment was developed to achieve therapeutic effects and minimize adverse effects, displaying "all-in-one" anti-tumor therapeutic efficacy both *in vivo* and *in vitro*. The synergistic approach resulted in significantly improving anti-tumor effects (with a tumor suppression rate increase from <5% by 5-FU only to 80.10%). The combined use of multiple alternative therapies has reduced the dosage of chemotherapy drugs and moderated the intensity and duration of PTT, thus minimizing side effects and ensuring safety. We aspire that the concept of appropriate combination in the design of multimodal therapies could inspire other tumor treatments, and the establishment of a multifunctional nanoplatform such as 5NiTiB could provide valuable insights for the rational design of drug delivery systems using 2D materials in the future.

Author contributions

Zhirong Zhang, Ling Zhang, and Yani Xu conceived this project. Yani Xu designed and carried out the experiments. Lan Yang, Min Li, Haozhou Shu, and Xiaojia Yang participated in part of the

experiments. Na Jia, Yunzhen Gao, and Rongying Shi provided the methodology supporting. Yani Xu performed data analysis and wrote the manuscript.

Conflicts of interest

All the authors have no conflicts of interest to declare.

Appendix A. Supporting information

Supporting data to this article can be found online at https://doi.org/10.1016/j.apsb.2023.10.005.

References

1. Gounder MM, Agaram NP, Trabucco SE, Robinson V, Ferraro RA, Millis SZ, et al. Clinical genomic profiling in the management of patients with soft tissue and bone sarcoma. *Nat Commun* 2022;**13**: 3406.
2. Ge YX, Zhang TW, Zhou L, Ding W, Liang HF, Hu ZC, et al. Enhancement of anti-PD-1/PD-L1 immunotherapy for osteosarcoma using an intelligent autophagy-controlling metal organic framework. *Biomaterials* 2022;**282**:121407.
3. Beird HC, Bielack SS, Flanagan AM, Gill J, Heymann D, Janeway KA, et al. Osteosarcoma. *Nat Rev Dis Prim* 2022;**8**:77.
4. Zhou Y, Yang D, Yang Q, Lv X, Huang W, Zhou Z, et al. Single-cell RNA landscape of intratumoral heterogeneity and immunosuppressive microenvironment in advanced osteosarcoma. *Nat Commun* 2020;**11**: 6322.
5. Meltzer PS, Helman LJ. New horizons in the treatment of osteosarcoma. *NEJM* 2021;**385**:2066−76.
6. Longhi A, Ferrari S, Tamburini A, Luksch R, Fagioli F, Bacci G, et al. Late effects of chemotherapy and radiotherapy in osteosarcoma and Ewing sarcoma patients: the Italian Sarcoma Group Experience (1983−2006). *Cancer* 2012;**118**:5050−9.
7. Zhao L, Zhang X, Wang X, Guan X, Zhang W, Ma J. Recent advances in selective photothermal therapy of tumor. *J Nanobiotechnol* 2021; **19**:335.
8. Wang Y, Meng HM, Li Z. Near-infrared inorganic nanomaterial-based nanosystems for photothermal therapy. *Nanoscale* 2021;**13**:8751−72.
9. Wang S, Li K, Chen Y, Chen H, Ma M, Feng J, et al. Biocompatible PEGylated MoS2 nanosheets: controllable bottom-up synthesis and highly efficient photothermal regression of tumor. *Biomaterials* 2015; **39**:206−17.
10. Shi M, Fu Z, Pan W, Chen Y, Wang K, Zhou P, et al. A protein-binding molecular photothermal agent for tumor ablation. *Angew Chem Int Ed* 2021;**60**:13564−8.
11. Zhang L, Li CX, Wan SS, Zhang XZ. Nanocatalyst-mediated chemodynamic tumor therapy. *Adv Healthcare Mater* 2022;**11**: e2101971.
12. Tang Z, Zhao P, Wang H, Liu Y, Bu W. Biomedicine meets Fenton chemistry. *Chem Rev* 2021;**121**:1981−2019.
13. Tang Z, Liu Y, He M, Bu W. Chemodynamic therapy: tumour microenvironment-mediated Fenton and Fenton-like reactions. *Angew Chem Int Ed* 2019;**58**:946−56.
14. Jia C, Guo Y, Wu FG. Chemodynamic therapy *via* Fenton and Fenton-like nanomaterials: strategies and recent advances. *Small* 2022;**18**: e2103868.
15. Lin LS, Huang T, Song J, Ou XY, Wang Z, Deng H, et al. Synthesis of copper peroxide nanodots for H2O2 self-supplying chemodynamic therapy. *J Am Chem Soc* 2019;**141**:9937−45.
16. Xiao Z, Zuo W, Chen L, Wu L, Liu N, Liu J, et al. H2O2 self-supplying and GSH-depleting nanoplatform for chemodynamic therapy synergetic photothermal/chemotherapy. *ACS Appl Mater Interfaces* 2021; **13**:43925−36.
17. Sangro B, Sarobe P, Hervás-Stubbs S, Melero I. Advances in immunotherapy for hepatocellular carcinoma. *Nat Rev Gastroenterol Hepatol* 2021;**18**:525−43.
18. Qiu B, Matthay KK. Advancing therapy for neuroblastoma. *Nat Rev Clin Oncol* 2022;**19**:515−33.
19. D'Angelo SP, Mahoney MR, Van Tine BA, Atkins J, Milhem MM, Jahagirdar BN, et al. Nivolumab with or without ipilimumab treatment for metastatic sarcoma (Alliance A091401): two open-label, non-comparative, randomised, phase 2 trials. *Lancet Oncol* 2018;**19**:416−26.
20. Li Z, Chu Z, Yang J, Qian H, Xu J, Chen B, et al. Immunogenic cell death augmented by manganese zinc sulfide nanoparticles for metastatic melanoma immunotherapy. *ACS Nano* 2022;**16**:15471−83.
21. Zhou G, Li M. Near-infrared-II plasmonic trienzyme-integrated metal-organic frameworks with high-efficiency enzyme cascades for synergistic trimodal oncotherapy. *Adv Mater* 2022;**34**:e2200871.
22. Szuplewska A, Kulpińska D, Dybko A, Jastrzębska AM, Wojciechowski T, Rozmysłowska A, et al. 2D Ti2C (MXene) as a novel highly efficient and selective agent for photothermal therapy. *Mat Sci Eng C-Mater* 2019;**98**:874−86.
23. Zhu Y, Wang Z, Zhao R, Zhou Y, Feng L, Gai S, et al. Pt Decorated Ti3C2Tx MXene with NIR-II light amplified nanozyme catalytic activity for efficient phototheranostics. *ACS Nano* 2022;**16**:3105−18.
24. Chen R, Hung SF, Zhou D, Gao J, Yang C, Tao H, et al. Layered structure causes bulk NiFe layered double hydroxide unstable in alkaline oxygen evolution reaction. *Adv Mater* 2019;**31**:e1903909.
25. Luengo CV, Crescitelli MC, Lopez NA, Avena MJ. Synthesis of layered double hydroxides intercalated with drugs for controlled release: successful intercalation of ibuprofen and failed intercalation of paracetamol. *J Pharmaceut Sci* 2021;**110**:1779−87.
26. Feng C, Wang F, Liu Z, Nakabayashi M, Xiao Y, Zeng Q, et al. A self-healing catalyst for electrocatalytic and photoelectrochemical oxygen evolution in highly alkaline conditions. *Nat Commun* 2021; **12**:5980.
27. Ho LWC, Liu Y, Han R, Bai Q, Choi CHJ. Nano-cell interactions of non-cationic bionanomaterials. *Acc Chem Res* 2019;**52**:1519−30.
28. Leroueil PR, Berry SA, Duthie K, Han G, Rotello VM, McNerny DQ, et al. Wide varieties of cationic nanoparticles induce defects in supported lipid bilayers. *Nano Lett* 2008;**8**:420−4.
29. Wang X, Cheng B, Zhang L, Yu J, Normatov I. Adsorption performance of tetracycline on NiFe layered double hydroxide hollow microspheres synthesized with silica as the template. *J Colloid Interface Sci* 2022;**627**:793−803.
30. Huang J, Xu Z, Jiang Y, Law WC, Dong B, Zeng X, et al. Metal organic framework-coated gold nanorod as an on-demand drug delivery platform for chemo-photothermal cancer therapy. *J Nanobiotechnol* 2021;**19**:219.
31. Anderson NM, Simon MC. The tumor microenvironment. *Curr Biol* 2020;**30**:R921. r5.
32. Qiu S, Zhang B, Wang X, Huang J, Zhao G, Ding M, et al. Interface strong-coupled 3D Mo-NiS@Ni-Fe LDH flower-cluster as exceptionally efficient electrocatalyst for water splitting in wide pH range. *J Colloid Interface Sci* 2023;**641**:277−88.
33. Huang Y, Liang J, Wang C, Yin S, Fu W, Zhu H, et al. Hybrid superlattices of two-dimensional materials and organics. *Chem Soc Rev* 2020;**49**:6866−83.
34. Deng D, Novoselov KS, Fu Q, Zheng N, Tian Z, Bao X. Catalysis with two-dimensional materials and their heterostructures. *Nat Nanotechnol* 2016;**11**:218−30.
35. Guo T, Chen L, Li Y, Shen K. Controllable synthesis of ultrathin defect-rich LDH nanoarrays coupled with MOF-derived Co-NC microarrays for efficient overall water splitting. *Small* 2022;**18**: e2107739.
36. Chen Z, Yun S, Wu L, Zhang J, Shi X, Wei W, et al. Waste-derived catalysts for water electrolysis: circular economy-driven sustainable green hydrogen energy. *Nano-Micro Lett* 2022;**15**:4.
37. Xue H, Thaivalappil A, Cao K. The potentials of methylene blue as an anti-aging drug. *Cells* 2021;**10**:3379.

38. Li X, Kong C, Chen Z. Colorimetric sensor arrays for antioxidant discrimination based on the inhibition of the oxidation reaction between 3,3′,5,5′-tetramethylbenzidine and hydrogen peroxides. *ACS Appl Mater Inter* 2019;**11**:9504−9.

39. Zheng X, Huang Q. Assessment of the antioxidant activities of representative optical and geometric isomers of astaxanthin against singlet oxygen in solution by a spectroscopic approach. *Food Chem* 2022;**395**:133584.

40. Cui X, Ruan Q, Zhuo X, Xia X, Hu J, Fu R, et al. Photothermal nanomaterials: a powerful light-to-heat converter. *Chem Rev* 2023;**11**:6891−952.

41. Famta P, Shah S, Jain N, Srinivasarao DA, Murthy A, Ahmed T, et al. Albumin-hitchhiking: fostering the pharmacokinetics and anticancer therapeutics. *J Control Release* 2023;**353**:166−85.

42. Zhang Y, Guo Z, Cao Z, Zhou W, Zhang Y, Chen Q, et al. Endogenous albumin-mediated delivery of redox-responsive paclitaxel-loaded micelles for targeted cancer therapy. *Biomaterials* 2018;**183**:243−57.

43. Lin T, Zhao P, Jiang Y, Tang Y, Jin H, Pan Z, et al. Blood−brain-barrier-penetrating albumin nanoparticles for biomimetic drug delivery *via* albumin-binding protein pathways for antiglioma therapy. *ACS Nano* 2016;**10**:9999−10012.

44. Jurak M, Wiącek AE, Ładniak A, Przykaza K, Szafran K. What affects the biocompatibility of polymers?. *Adv Colloid Interface Sci* 2021;**294**:102451.

45. Bazhin AA, Sinisi R, De Marchi U, Hermant A, Sambiagio N, Maric T, et al. A bioluminescent probe for longitudinal monitoring of mitochondrial membrane potential. *Nat Chem Biol* 2020;**16**:1385−93.